

# Design and evaluation of a hybrid photoacoustic tomography and diffuse optical tomography system for breast cancer detection

Lei Xi, Xiaoqi Li, and Lei Yao

Department of Biomedical Engineering, University of Florida, Gainesville, Florida 32611

Stephen Grobmyer

Department of Surgery, University of Florida, Gainesville, Florida 32611

Huabei Jiang<sup>a)</sup>

Department of Biomedical Engineering, University of Florida, Gainesville, Florida 32611

(Received 2 January 2012; revised 27 March 2012; accepted for publication 28 March 2012; published 18 April 2012)

**Purpose:** The authors present the design and evaluation of a second-generation (G2) hybrid photoacoustic tomography (PAT) and diffuse optical tomography (DOT) imaging system for detection of breast cancer. The combined PAT/DOT system takes full advantages of two different modalities to provide complementary information and most accurate recovery of tissue optical properties.

**Methods:** This system was designed to produce cross-section images of breast tissue with a ring-shaped home-made array of 64 wideband acoustic transducers combined with an array of 16/16 source/detector optical fiber bundles. A scanning light delivery system was built to illuminate a large area of breast tissue for optimized tissue penetration. Finite element reconstruction methods for quantitative PAT and DOT were utilized to recover absorption and scattering coefficients of tissue-mimicking phantoms and *ex vivo* tumor tissue.

**Results:** Performances of the acoustic transducer array and the PAT/DOT system were investigated in detail. Frequency response of the transducers is from 380 kHz to 1.48 MHz and maximum frequency response is up to 2 MHz. Directivity of a single element in the array is  $\pm 30^\circ$ . The PAT/DOT system offers a spatial resolution of  $\sim 0.5$  mm for PAT and of  $\sim 4.0$  mm for DOT. Quantitatively accurate absorption and scattering coefficients were obtained from both the phantom and *ex vivo* experiments.

**Conclusions:** The PAT/DOT system provided better PAT images when the targets were smaller in size and located near the center of the background phantom, while better DOT images were obtained when the targets were larger in size and located away from the center of the background. The successful results obtained from both the phantom and *ex vivo* experiments will allow us to test the hybrid system in humans with breast cancer in the near future. © 2012 American Association of Physicists in Medicine. [http://dx.doi.org/10.1118/1.3703598]

Key words: photoacoustic tomography, diffuse optical tomography, breast cancer

## I. INTRODUCTION

Breast cancer is the second most important public health problem, which affects one in four women in the United States.<sup>1</sup> While x-ray mammography is the current clinical tool for screening and diagnosis of breast cancer,<sup>2</sup> it has numerous limitations such as the inability of imaging dense breast and the use of ionization radiation. Among various techniques being developed to overcome the limitations associated with x-ray,<sup>3–9</sup> diffuse optical tomography (DOT) and photoacoustic tomography (PAT) are particularly interesting and promising. DOT can provide both tissue functional information and cellular morphology,<sup>10</sup> while PAT can offer high resolution tissue function information.

In PAT, a single short-pulsed light beam illuminates an object and the photoacoustic waves excited by thermoelastic expansion due to optical absorption are measured using wide-band ultrasound transducer(s); hence, optical absorption or functional parameters can be obtained with ultrasound resolution. To date, several PAT systems for breast cancer detection

have been reported. Oraevsky and co-workers<sup>7</sup> developed a laser-based photoacoustic imaging system (LOIS) with an arch-shaped 64-element acoustic array capable of providing a spatial resolution of 1 mm. Haisch *et al.*<sup>6</sup> reported a combined photoacoustic and ultrasound imaging system. Manohar *et al.*<sup>8</sup> built a three-dimensional PAT system that could cover a 90 mm field of view. In their system, a planar array of 590 PVDF transducers was used, offering a spatial resolution of 2.3–3.9 mm given an imaging depth of up to 32 mm. Pramanik *et al.*<sup>11</sup> described a hybrid PAT and thermoacoustic tomography system. Kruger *et al.*<sup>12</sup> recently reported an interesting PAT study of breast angiography using a  $64 \times 64 \times 50$  mm field of view given a 40 mm imaging depth.

While the results from these studies are promising, PAT has limitations. For example, PAT can provide high quality images only for certain size of targets due to the limited detection band of an ultrasound transducer. It is difficult to accurately detect a relatively large size target (e.g.,  $\geq 6$  mm) using a typical  $\geq 1$  MHz transducer. In addition, the limited directivity of a transducer may lead to imbalanced image quality for

the entire imaging area/volume. Yet, it still remains a major challenge for PAT to recover tissue scattering coefficient, an important parameter for breast cancer detection.<sup>10</sup>

DOT is capable of overcoming the above mentioned limitations associated with PAT, although it has relatively a low spatial resolution. Thus, a combination of PAT and DOT appears to be an ideal approach for breast imaging. Toward this, we recently reported for the first time a hybrid system that integrated PAT and DOT in a single platform.<sup>13</sup> The goal of the current work is to develop an improved G2 PAT/DOT system using a ring-shaped 64-element array with improved sensitivity and directivity over the previous 32-element array used in our first prototype. The G2 PAT/DOT is validated using phantom and *ex vivo* experiments.

## II. MATERIAL AND METHODS

### II.A. System description

Figure 1(a) presents the schematic of our PAT/DOT hybrid system. Detailed description of the DOT part has been reported previously.<sup>5</sup> Briefly, light generated from a diode laser is delivered sequentially by an optical switch and optical fiber bundles to 16 source positions. For each source position, diffused light is detected by 16 detection fiber bundles coupled with detection units and data acquisition board and used for DOT image reconstruction.

For the PAT part, a pulsed light from a Nd:YAG or Ti:Sapphire laser with a 6 ns pulse duration and 10 Hz repetition rate is sent to the object through a light delivery system.

The laser-generated ultrasound signals are collected by 64 transducers, which are connected via a mechanic switching system to a 16-channel preamplifier and 16-channel data acquisition (DAQ) board. The sampling rate of the DAQ board triggered by the laser is 50 MHz.

As shown in Fig. 1(b), the finished optical fibers/transducers/object interface contains a homemade 64-elements acoustic transducer array. We used commercial PVDF film (110  $\mu\text{m}$ ) with silver electrode in both sides. The film was shaped into 32 rectangle units with a size of  $5 \times 30$  mm. For each unit, a hole in the center was drilled for the placement of a fiber bundle of DOT. The positive electrode was divided into two parts with an equal size of  $2.3 \times 30$  mm, and the PVDF film was attached to backing material with the same size as the film by transparent epoxy resin. The positive and negative electrodes of a coaxial cable were connected to the film using silver epoxy. A copper housing was used to shield electromagnetic noise for each unit to improve the signal-to-noise ratio.

#### II.A.1. Light delivery system

We initially tested a fiber bundle based light delivery approach and found it was not feasible since the damage threshold for a typical fiber bundle was 20 mJ, which was much lower than the at least 60 mJ needed for us to illuminate an object area of 3  $\text{cm}^2$  (calculated based on the maximum

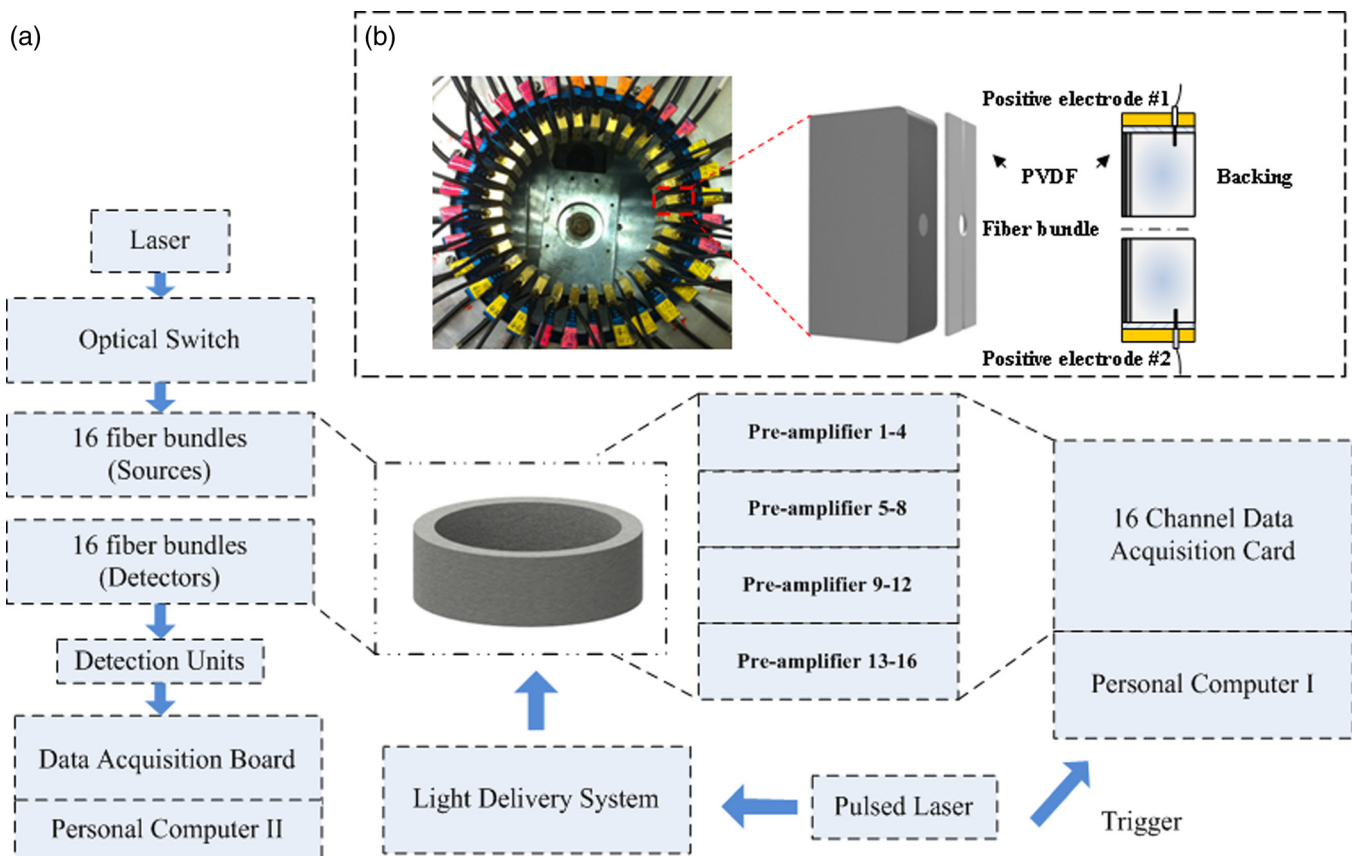


FIG. 1. (a) Schematic of the PAT/DOT system. (b) Photograph of the interface and schematic of a single transducer.

permissible exposure to light for human tissue surface). Therefore, we developed a light delivery system by mounting three prisms to a two-dimensional step motor [Fig. 2(a)]. A concave lens and ground glass indicated by arrow 3 in Fig. 2(a) were attached to the front of output end of the light delivery system to extend the light beam to be 3 cm<sup>2</sup>. The output laser beam was delivered from bottom of the examination table to the phantom. During an imaging experiment, the light beam is scanned in two-dimension [arrows 1 and 2 in Fig. 2(a)] via two step motors to realize the light illumination to cover a large area.

**II.A.2. Frequency response of transducers**

Ultrasound signal generated by photoacoustic affect on a sphere absorber is distributed in bipolar shape and the Fourier spectrum of this signal reveals the major frequency components the acoustic energy contains. Therefore, the frequency

bandwidth of the transducer determines the detectable range of target size. We used an impulsive wave method described by Manohar *et al.*<sup>8</sup> to measure the frequency response of each element. Figure 2(b) shows that the -6 dB bandwidth of the transducer is from 380 kHz to 1.48 MHz and maximum frequency response is up to 2 MHz.

**II.A.3. Directivity and sensitivity of transducers**

Figure 2(c) presents the directivity of a transducer measured in the plane parallel to the short side of the transducer. It was estimated to be  $\pm 30^\circ$  based on the -6 dB level. The methodology we used for the estimation was described by Ermilov *et al.*<sup>7</sup> The normalized sensitivity for the 64 elements is shown in Fig. 2(d) where we see that the sensitivity lied in the range of 0.7–1.0. We used this set of data to calibrate the measurements from each element for image reconstruction.

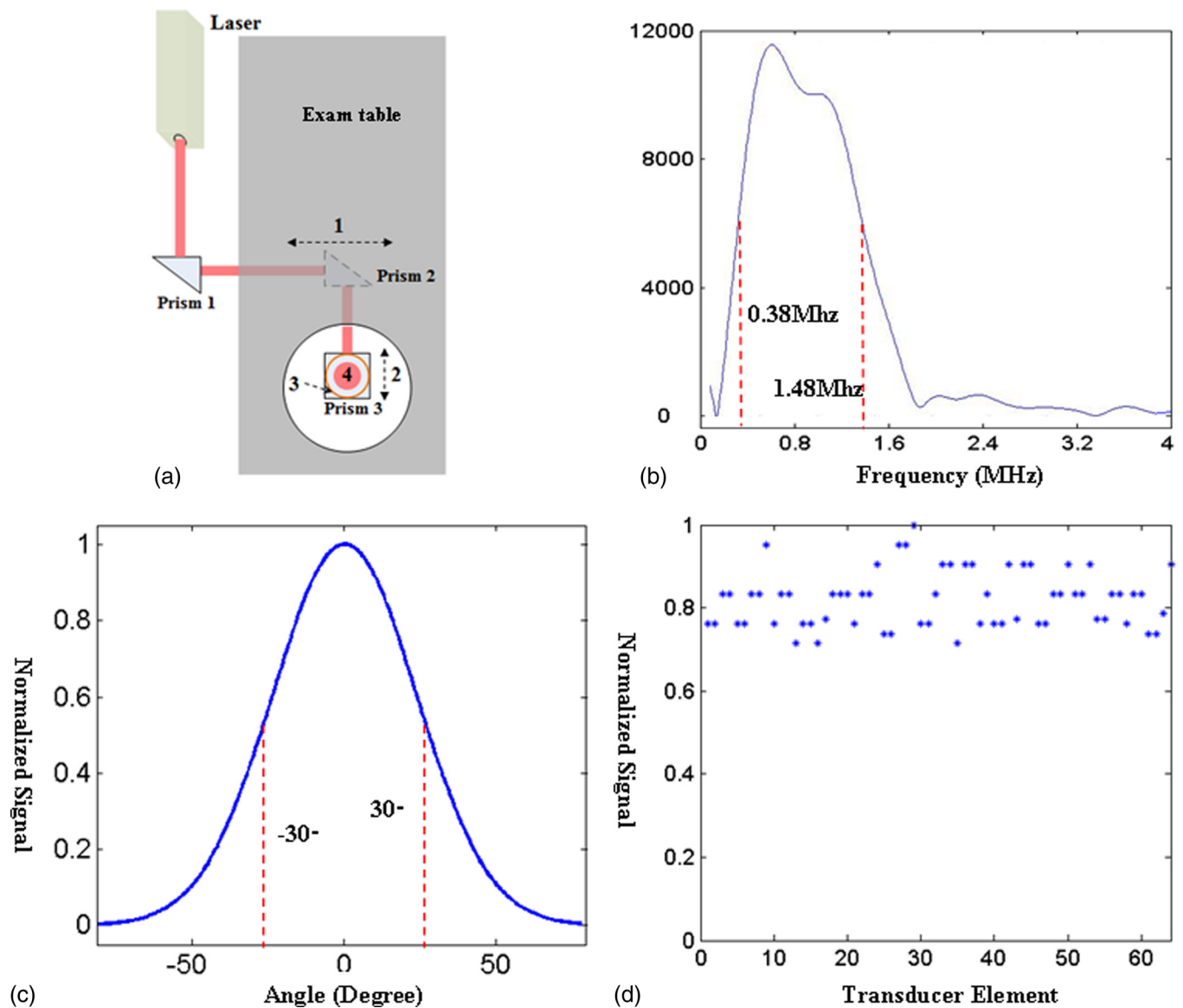


FIG. 2. (a) 3D schematic of the light delivery system. (b) Frequency response of a transducer. Dashed line shows the -6 dB level. (c) Directivity of a transducer. Dashed line shows the -6 dB level. (d) Normalized sensitivity for all the elements in the transducer array.

**II.B. Quantitative reconstruction algorithms**

Various quantitative reconstruction methods have been explored for PAT and DOT. The reconstruction methods for both PAT and DOT in our PAT/DOT system are finite element (FE) based.

For PAT, the FE-based dual-meshing reconstruction algorithm described by Yao *et al.*<sup>14</sup> was used to recover absorption coefficient from the photoacoustic measurements. The algorithm includes two steps. The first is to obtain the map of the absorbed optical energy density. The second step is to recover the distribution of the absorption coefficient from the absorbed energy density. The core procedure of our PAT reconstruction algorithm can be described by the following two equations:

$$\nabla^2 p(r, \omega) + k_0^2 p(r, \omega) = ik_0 \frac{c_0 \beta \Phi(r)}{C_p}, \tag{1}$$

$$(\mathfrak{I}^T \mathfrak{I} + \lambda I) \Delta \chi = \mathfrak{I}^T (p^0 - p^c), \tag{2}$$

where  $p$  is the pressure wave;  $k_0 = \omega/c_0$  is the wave number described by the angular frequency,  $\omega$ , and the speed of the acoustic wave in the medium,  $c_0$ ;  $\beta$  is the thermal expansion coefficient;  $C_p$  is the specific heat;  $\Phi$  is the absorbed energy density that is the product of the absorption coefficient,  $\mu_a$ , and optical fluence,  $\Psi$  (i.e.,  $\Phi = \mu_a \Psi$ );  $p^0 = (p_1^c, p_2^c, \dots, p_M^c)^T$ , and  $p_i^0$  and  $p_i^c$  are the observed and computed complex acoustic field data for  $i = 1, 2, \dots, M$  boundary locations;  $\Delta \chi$  is the update vector for the absorbed optical energy density;  $\mathfrak{I}$  is the Jacobian matrix formed by  $\partial p / \partial \Phi$  at the boundary measurement sites;  $\lambda$  is the regularization parameter determined by combined Marquardt and Tikhonov regularization schemes; and  $I$  is the identity matrix. Thus, here the image

formation task is to update the absorbed optical energy density distribution via the iterative solution of Eqs. (1) and (2), so that an object function composed of a weighted sum of the squared difference between the computed and measured acoustic data can be minimized. The second step is based on the iterative solution to the following radiation transport equation (RTE):

$$(\bar{\Omega} \cdot \nabla + \mu_s + \mu_a) \varphi(\bar{r}, \bar{\Omega}) = \mu_s \int_{S^{n-1}} \varphi(\bar{r}, \bar{\Omega}') \Theta(\bar{\Omega}, \bar{\Omega}') d\bar{\Omega}' + q(\bar{r}, \bar{\Omega}), \tag{3}$$

where  $\mu_s$  is the scattering coefficient;  $\varphi(\bar{r}, \bar{\Omega})$  is the radiance;  $q(\bar{r}, \bar{\Omega})$  is the source term;  $\bar{\Omega} \in S^{n-1}$  denotes a unit vector in the direction of interest. The kernel  $\Theta(\bar{\Omega}, \bar{\Omega}')$  is the scattering phase function describing the probability density that a photon with an initial direction  $\bar{\Omega}'$  will have a direction  $\bar{\Omega}$  after a scattering event. If the incident laser source strength and the absorbed energy density are estimated in advance, absorption coefficient distribution can be determined by iterative solution procedure using the finite element method. In the PAT reconstruction,  $\mu_s$  are assumed constant in this study. A fine mesh of 6285 nodes and a coarse mesh of 1604 nodes were applied in the reconstruction, and the images were converged within 50 iterations using a parallel computer.

For DOT, both the absorption and scattering coefficient images were recovered from the algorithms described in detail by Li and Jiang<sup>15</sup> and Jiang *et al.*<sup>16</sup> In short, the algorithms use a regularized Newton's method to update an initial optical property distribution iteratively in order to minimize an object function composed of a weighted sum of the squared difference between computed and measured optical data at the medium surface. The computed optical data

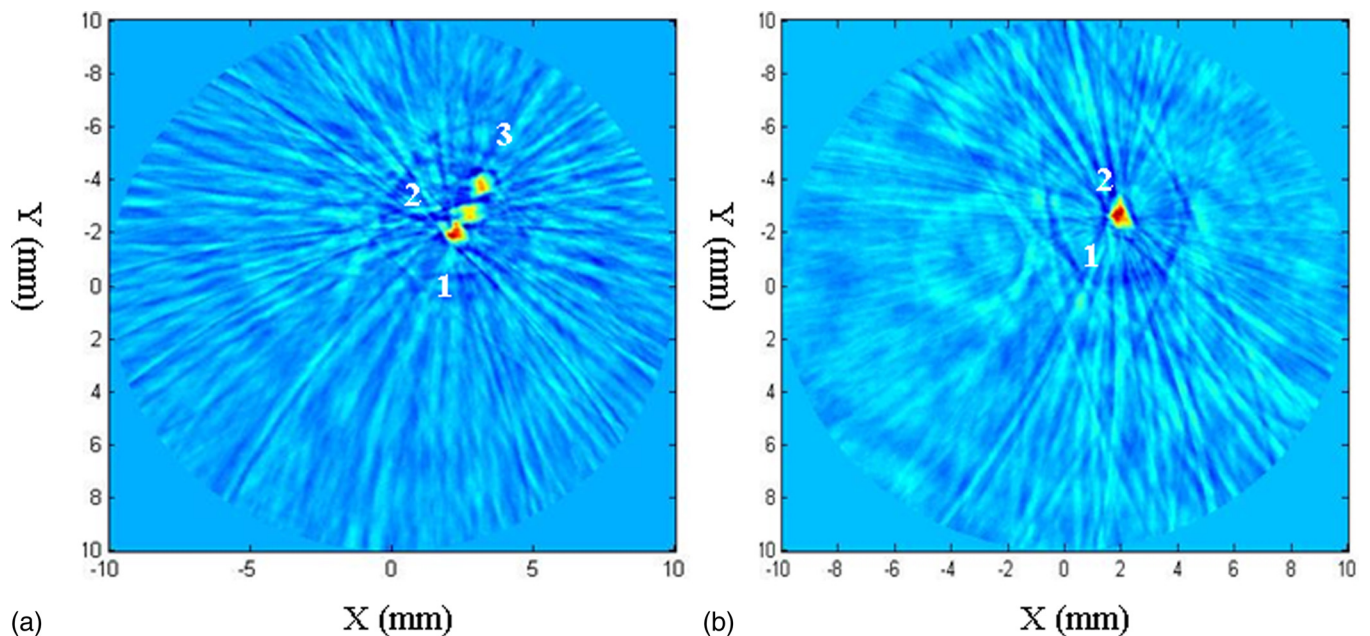


FIG. 3. (a) PAT image of three separated metal wires (0.15 mm in diameter each) embedded in the phantom background. (b) PAT image of two metal wires (0.15 mm in diameter each) placed in the phantom background.

TABLE I. Exact size (diameter), location (off center), depth, and absorption and reduced scattering coefficients of the five targets.

	Size (mm)	Location (mm)	Depth <sup>a</sup> (mm)	$\mu_a$ (mm <sup>-1</sup> )	$\mu'_s$ (mm <sup>-1</sup> )
Target 1	4	0	0 (22)	0.028	2
Target 2	4	20	5 (15)	0.028	2
Target 3	6	30	5 (10)	0.028	2
Target 4	6	20	5 (15)	0.028	2
Target 5	2	20	5 (15)	0.028	2

<sup>a</sup>The maximum experimental imaging depth for certain cases is given in the parenthesis.

(i.e., photon density) is obtained by solving the photon diffusion equation with a finite element method. The core procedure in our reconstruction algorithms is to iteratively solve the following regularized matrix equation:

$$(\mathfrak{I}^T \mathfrak{I} + \lambda I) \Delta q = \mathfrak{I}^T (\Phi^{(m)} - \Phi^{(c)}), \tag{4}$$

where  $\Phi$  is the photon density,  $I$  is the identity matrix, and  $\lambda$  can be a scalar or a diagonal matrix.  $\Delta q = (\Delta D_1, \Delta D_2, \dots, \Delta D_N, \Delta \mu_{a,1}, \Delta \mu_{a,2}, \dots, \Delta \mu_{a,N})^T$  is the update vector for the optical property profiles, where  $N$  is the total number of nodes in the finite element mesh used, and  $D$  is the diffusion coefficient.  $\Phi^{(m)} = (\Phi_1^{(m)}, \Phi_2^{(m)}, \dots, \Phi_M^{(m)})$  and  $\Phi^{(c)} = (\Phi_1^{(c)}, \Phi_2^{(c)}, \dots, \Phi_M^{(c)})$ , where  $\Phi_i^{(m)}$  and  $\Phi_i^{(c)}$ , respectively, are measured and calculated data for  $i = 1, 2, \dots, M$  boundary locations.  $\mathfrak{I}$

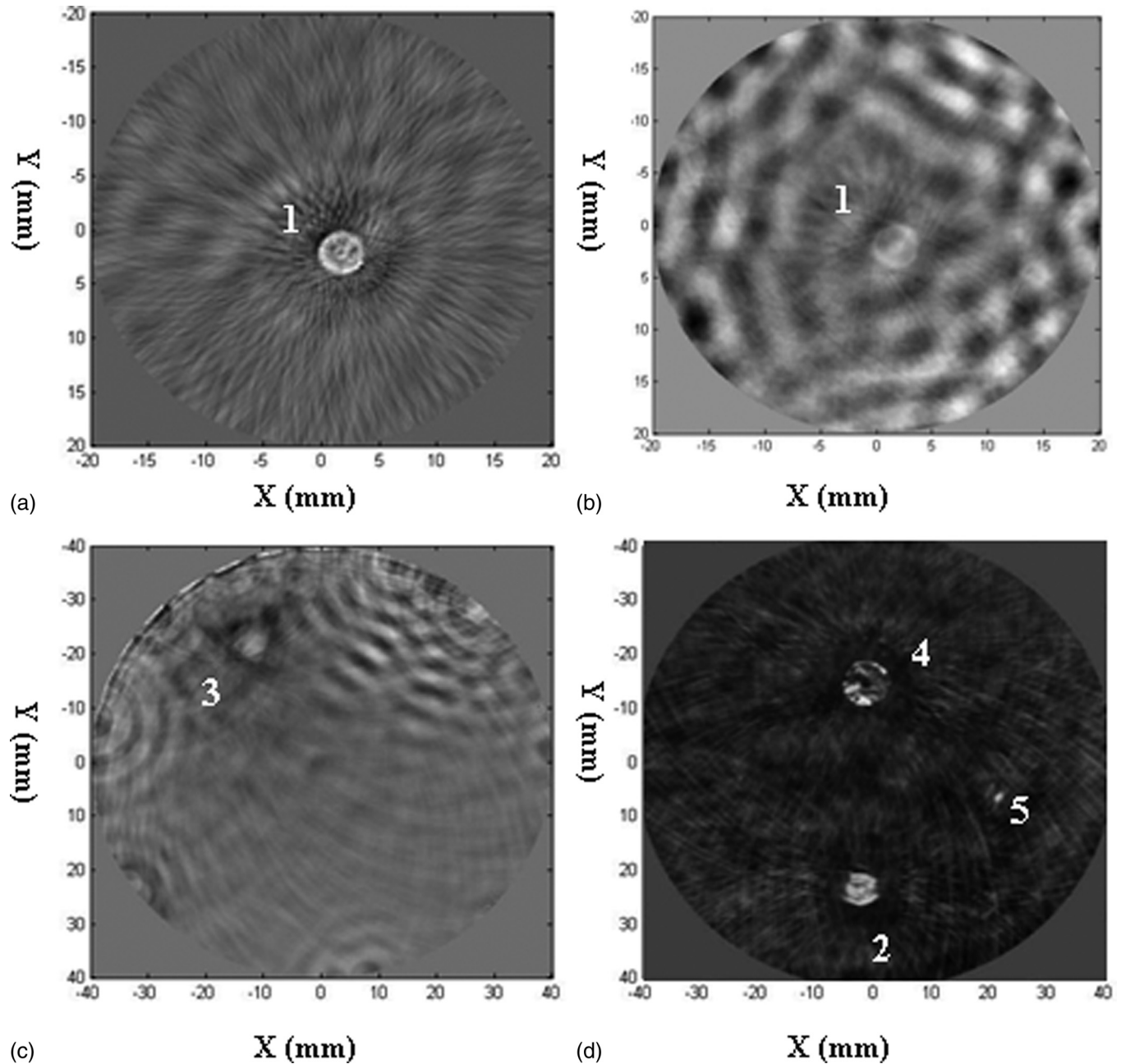


FIG. 4. (a) PAT image of target 1 without any depth. (b) PAT image of target 1 positioned at 22 mm beneath the surface. (c) PAT image of target 3 (30 mm off center positioned). (d) Fused image of multiple targets.

is the Jacobian matrix that is formed by  $\partial\Phi/\partial D$  and  $\partial\Phi/\partial\mu_a$  at the boundary measurement sites. In DOT, the goal is to update the  $\mu_a$  and  $D$  or  $\mu'_s$  distributions through the iterative solution of Eq. (4) so that a weighted sum of the squared difference between computed and measured data can be minimized. A single mesh of 700 nodes was used, and the images were converged within 15 iterations in a 3 GHz PC with 1 GB memory.

### III. RESULTS AND DISCUSSION

Since detailed system performance for DOT has been evaluated previously,<sup>5</sup> here, we focus on evaluating the PAT part of the PAT/DOT system on the imaging depth, active imaging area, and multitarget imaging ability using the light delivery system and conduct a comparison between PAT and DOT in these areas. We also test our PAT/DOT system using *ex vivo* tumor tissue embedded in a tissue-mimicking phantom.

#### III.A. Spatial resolution of the system

Spatial resolution of a PAT system is determined by several factors including the number of transducers, interelement spacing, and sensitivity and frequency response of the transducer as well as the reconstruction methods used.<sup>17,18</sup> Two experiments were performed to estimate the best spatial resolution of our system. In the first experiment, we put three thin metal wires (0.15 mm in diameter each) in the center of a phantom background. The distance was 0.5 and 0.7 mm, respectively, between wires 1 and 2 and between wires 2 and 3. In the second experiment, we placed two metal wires into the phantom background and the distance between the two wires was 0.3 mm. The reconstructed PAT images from the two experiments are shown in Figs. 3(a) and 3(b), respectively, where we note that the three targets can be clearly distinguished [Fig. 3(a)], while the two targets are not resolvable [Fig. 3(b)]. Hence, we determine that the best spatial resolution of our system is 0.5 mm.

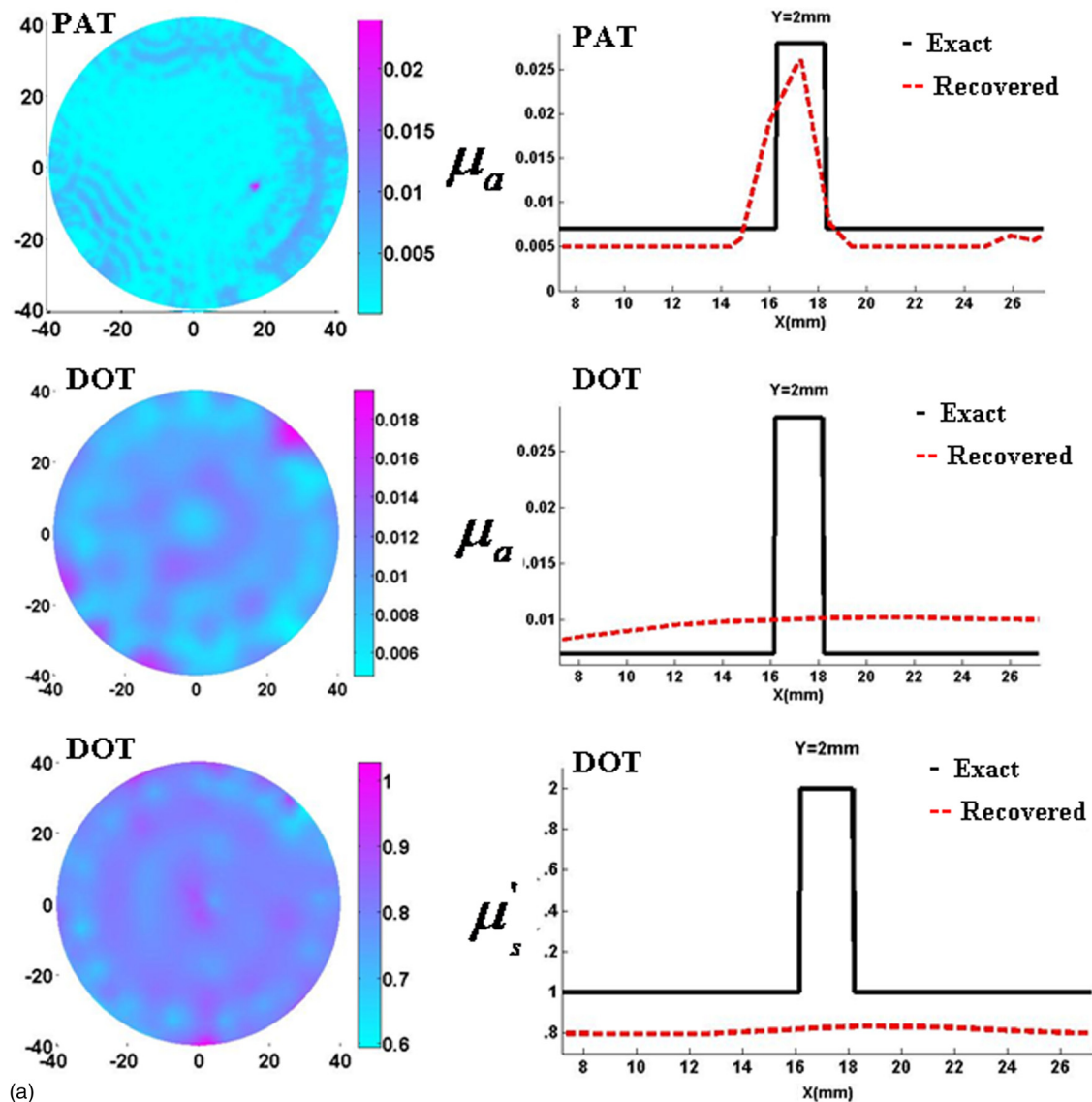


Fig. 5. Quantitative PAT and DOT images of target 5 (a), target 2 (b), target 3 (c), and target 6 (d).

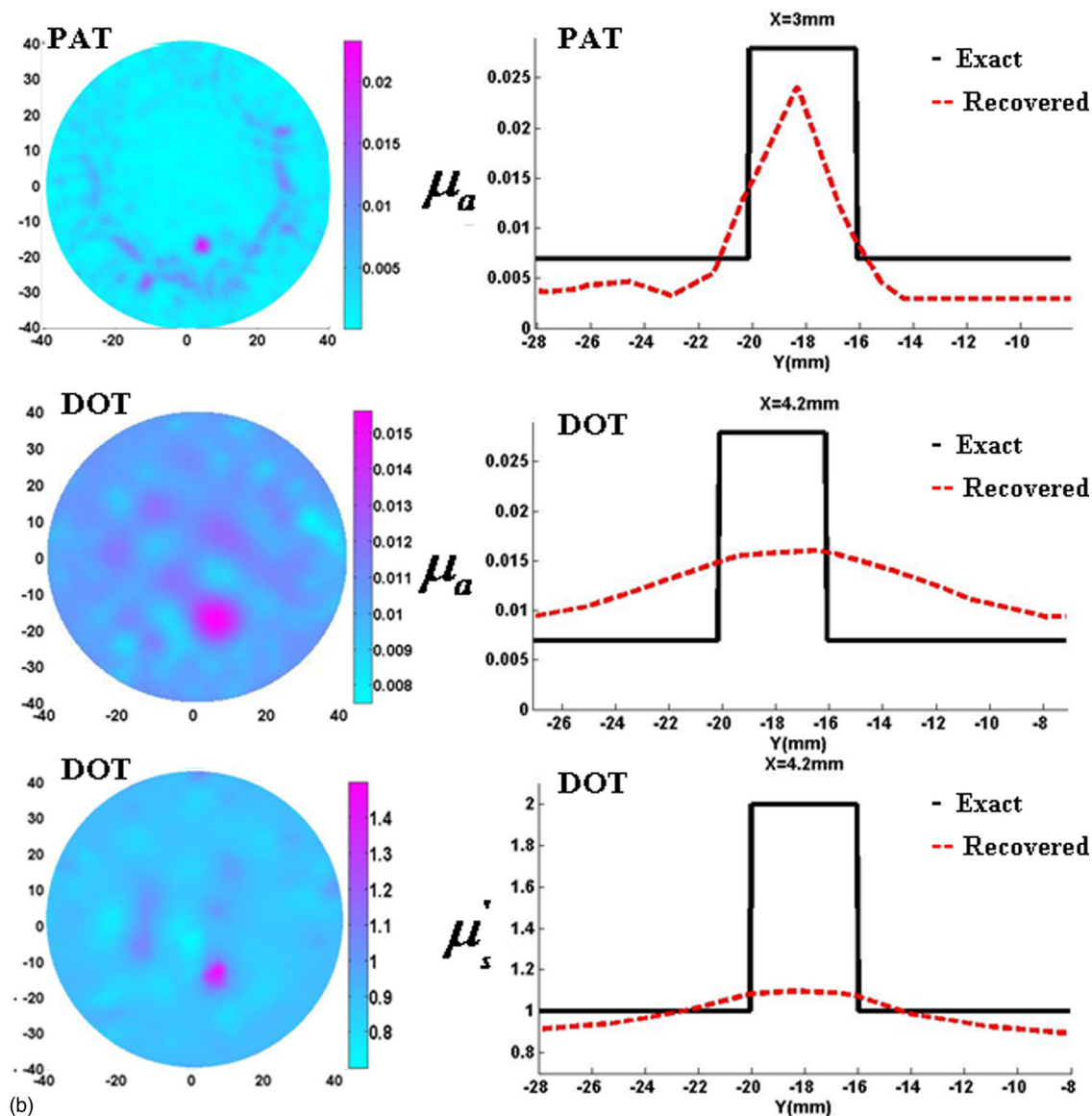


FIG. 5. (Continued)

### III.B. PAT performance

The detail parameters of the tissue-mimicking phantom (Intralipid + India ink) and five targets used for evaluating the PAT performance are listed in Table I. These experiments were performed using the 532 nm Nd:YAG pulsed laser. The light beam was guided and extended by our light delivery system to be an area source of  $3\text{ cm}^2$  and the PAT images were reconstructed by a delay and sum method.<sup>19</sup> The light energy density at the surface of the phantom was  $20\text{ mJ/cm}^2$ .

Figures 4(a) and 4(b) show the PAT images of target 1 located at 0 and 22 mm below the phantom surface, respectively. While the target is clearly better imaged with 0 mm depth, the target with 22 mm depth is still detectable. To detect a 2 mm-radius centrally located target, we found that the maximum depth was 7 and 22 mm for the G1 and G2 systems, respectively. In addition, due to the use of electromag-

netic shielding cases for the transducers in the G2 system, the signal needed not to be averaged while it needed to be averaged 100 times for the G1 system. The active imaging area for PAT is validated by the result shown in Fig. 4(c) where target 3 (30 mm off center positioned) is detected. Due to the limited directivity of transducers, we note that the shape of reconstructed target was distorted and stronger artifacts were seen around the target. We also tested and found that, when a target was placed at a  $>30$  mm off center position, the image quality became unacceptable. For the single target experiments, the light beam was directly delivered to the target area without scanning. The image shown in Fig. 4(d) demonstrated the ability of imaging multiple targets using the developed light delivery system. Three targets (2, 4, and 5) separated with a large distance were imaged by scanning the laser beam nine ( $3 \times 3$ ) times to cover the whole phantom surface. The nine images obtained from the nine laser beam positions were then fused into a single image shown in Fig. 4(d).

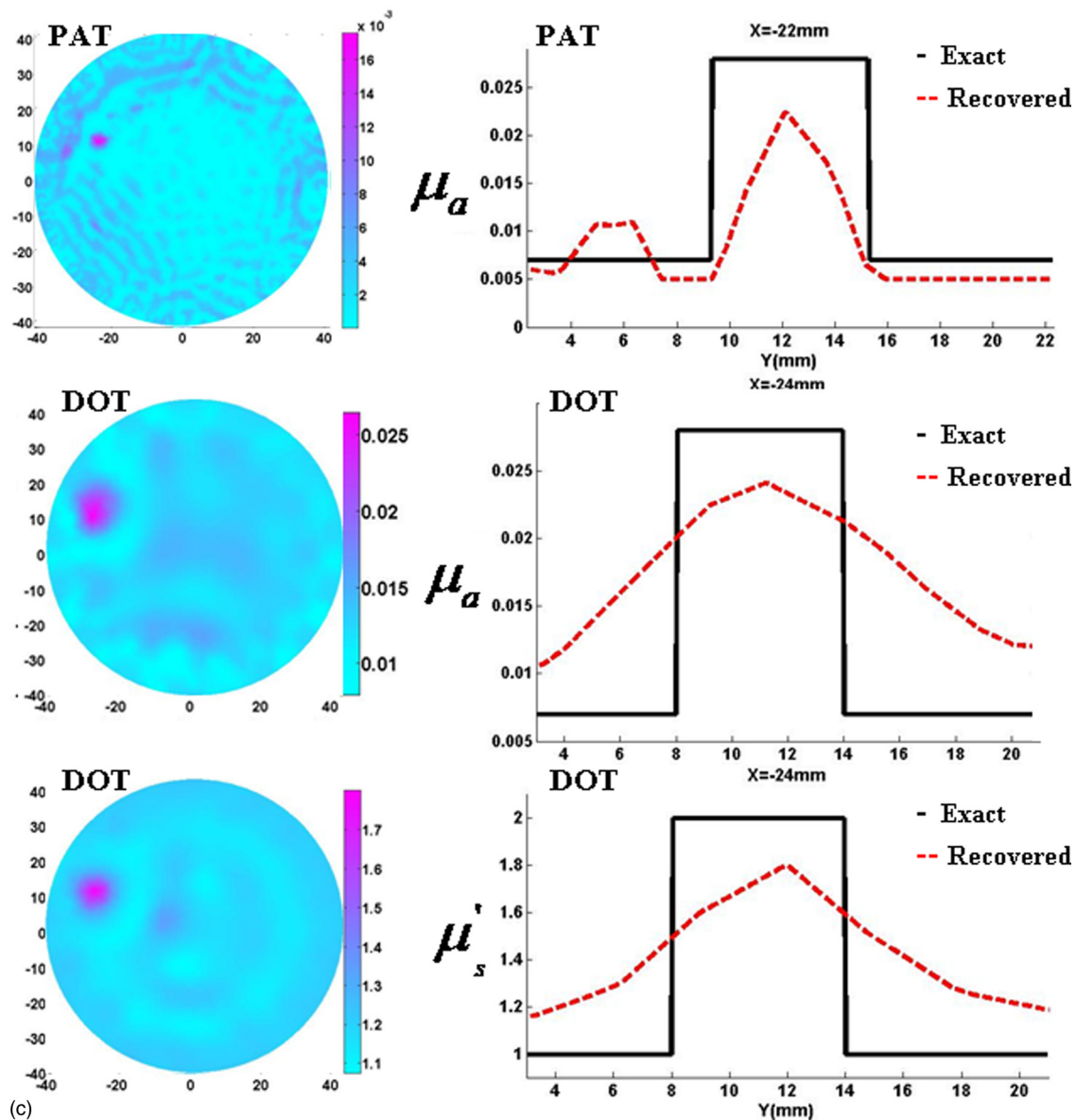


FIG. 5. (Continued)

### III.C. PAT and DOT comparison

Figure 5 presents the reconstructed quantitative absorption coefficient images by PAT and absorption and scattering coefficient images by DOT for some of targets 1–5 and for a relatively large target, target 6 positioned 20 mm off center (radius = 5 mm, absorption coefficient =  $0.028 \text{ mm}^{-1}$ , and scattering coefficient =  $4.0 \text{ mm}^{-1}$ ). These quantitative images were recovered using our finite element based PAT and DOT. Figure 5 also gives the reconstructed optical property profiles depicted along one cut line crossing through the center of the target (red dashed line) for each case in comparison with the exact property values (black solid line).

From Fig. 5(a), we see that target 5 (radius = 1 mm) is accurately recovered by PAT in terms of its size, position, and absorption coefficient value, while it is not detectable by DOT in both the absorption and scattering images. For target 2 (radius = 2 mm), again PAT can accurately reconstruct its

size, position, and absorption coefficient value [Fig. 5(b)]. In this case, DOT can detect the target from both the absorption and scattering images; however, the values of both absorption and scattering coefficients are significantly underestimated. Figure 5(c) shows that target 3 (radius = 3 mm) is quantitatively recovered by both PAT and DOT while we note an overestimated target size by DOT.

Interestingly, the largest target 6 (radius = 5 mm) is poorly recovered by PAT [Fig. 5(d)], due to the loss of low frequency signals given the limited frequency response of the transducers. Here, we see that only the edge of the target is recovered by PAT and the reconstructed absorption coefficient value is considerably underestimated. DOT in this case provides accurate recovery of the target in terms of its size, position, and absorption and scattering coefficient values.

Overall from the results shown in Fig. 5 and the summary in Table II, PAT can provide both qualitatively and quantitatively better images than DOT when the target size is equal

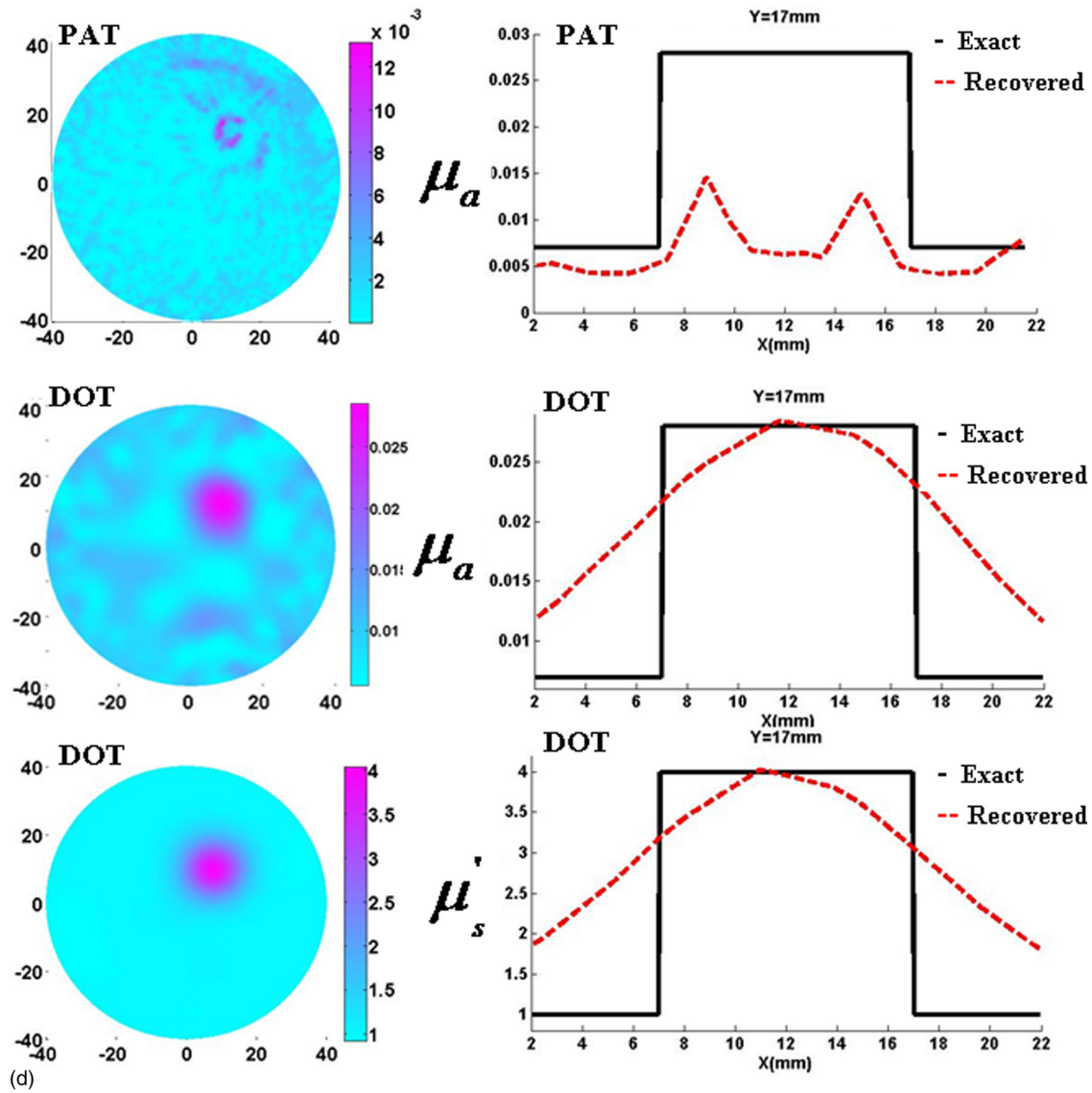


FIG. 5. (Continued)

to or small than 3 mm in radius, while DOT can offer better image quality when the target size is larger than 3 mm in radius. We also notice that the smallest detectable target size is 2 mm in radius for DOT given the experimental conditions used in this study.

**III.D. Ex vivo experiment**

For the *ex vivo* experiment, a tumor was removed from a rat bearing a 4T1 tumor of approximately 3.5 mm in radius and embedded in the phantom background. In this case, 730 nm pulsed light from a Ti:Sapphire laser was employed and provided an energy density of 20 mJ/cm<sup>2</sup> at the phantom surface. Figure 6 shows the recovered absorption and/or scattering images where we see that the tumor is detected by both PAT and DOT. The absorption coefficient of the tumor recovered by PAT is consistent with that by DOT. Through quantitative analysis of *ex vivo* PAT and DOT images, the size of tumor (3 mm in radius) estimated by the absorption image of

TABLE II. Exact and reconstructed target size (diameter), location (off center), and absorption and reduced scattering coefficients for the phantom experiments.

		Size (mm)	$\mu_a$ (mm <sup>-1</sup> )	$\mu'_s$ (mm <sup>-1</sup> )	Location (mm)
Case 1	Exact	2	0.028	2	20
	PAT	2	0.026	NA	20
	DOT	NA	NA	NA	20
Case 2	Exact	4	0.028	2	20
	PAT	4	0.025	NA	20
	DOT	10	0.017	1.1	20
Case 3	Exact	6	0.028	2	20
	PAT	6	0.024	NA	20
	DOT	10	0.024	1.8	20
Case 4	Exact	10	0.028	4	20
	PAT	8	0.015	NA	20
	DOT	12	0.028	4	20

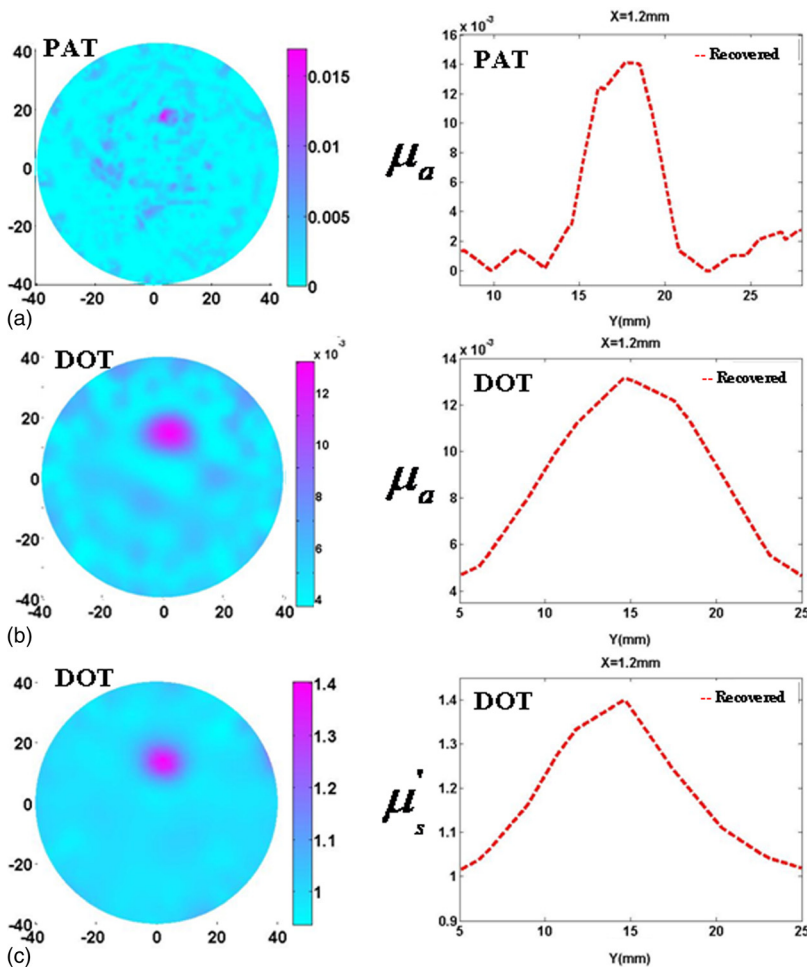


FIG. 6. Reconstructed *ex vivo* absorption image by PAT (a) and absorption (b) and scattering (c) images by DOT.

PAT and by the scattering image of DOT is consistent with the actual tumor size, while it is overestimated by the absorption image of DOT to be 5 mm in radius.

#### IV. CONCLUSIONS

We have developed a second generation prototype PAT/DOT system and evaluated its validity using phantom and *ex vivo* tumor experiments. This system takes full advantages of both PAT and DOT to provide high resolution absorption image and scattering image. While we plan to test this system in breast cancer patients in the near future, we are aware that there are still several improvements that need to be undertaken before this testing. First, multispectral PAT imaging will be considered to provide tissue functional information. Second, we will use the absorption coefficient recovered by PAT as *a priori* knowledge to improve the scattering image reconstruction by DOT or use the scattering coefficient provided by DOT to enhance the absorption recovery of PAT. Third, the data acquisition for PAT will be improved by using a fast electronic switch with in-board pre-amplifiers that connects between the 64 transducers and the 16-channel data acquisition board. Finally, we note that when the light beam was delivered to the region near the boundary where the transducers are located, the acoustic signal generated by light delivered to

the surface of PVDF film resulted in notable artifacts in the reconstructed photoacoustic images. We are currently investigating some ways to minimize this effect including attaching a thin layer to the transducer to absorb the light and preprocessing the photoacoustic signals using wavelet transform before reconstruction.

#### ACKNOWLEDGMENTS

This research was supported in part by the Bankhead Coley Florida Cancer Research Program and by the J. Crayton Pruitt Family Endowment.

<sup>a)</sup> Author to whom correspondence should be addressed. Electronic mail: hjiang@bme.ufl.edu

<sup>1</sup> American Cancer Society, *Cancer Facts and Figures 2008* (American Cancer Society, Atlanta, GA, 2008).

<sup>2</sup> P. A. Carney *et al.*, "Individual and combined effects of age, breast density, and hormone replacement therapy use on the accuracy of screening mammography," *Ann. Intern. Med.* **138**(3), 168–175 (2003).

<sup>3</sup> D. Saslow *et al.*, "American Cancer Society guidelines for breast screening with MRI as an adjunct to mammography," *Ca-Cancer J. Clin.* **57**, 75–89 (2007).

<sup>4</sup> B. J. Tromberg *et al.*, "Assessing the future of diffuse optical imaging technologies for breast cancer management," *Med. Phys.* **35**(6), 2443–2451 (2008).

<sup>5</sup> C. Li, H. Zhao, B. Anderson, and H. Jiang, "Multispectral breast imaging using a ten-wavelength, 64 x 64 source/detector channels silicon photodiode-based diffuse optical tomography system," *Med. Phys.* **33**(3), 627–636 (2006).

- <sup>6</sup>C. Haisch *et al.*, "Combined optoacoustic/ultrasound system for tomographic absorption measurements: Possibilities and limitations," *Anal. Bioanal. Chem.* **397**, 1503–1510 (2010).
- <sup>7</sup>S. A. Ermilov *et al.*, "Laser optoacoustic imaging system for detection of breast cancer," *J. Biomed. Opt.* **14**(2), 024007 (2009).
- <sup>8</sup>S. Manohar, A. Kharine, J. C. G. van Hespren, W. Steenbergen, and T. G. van Leeuwen, "Photoacoustic mammography laboratory prototype: Imaging of breast tissue phantoms," *J. Biomed. Opt.* **9**, 1172–1181 (2004).
- <sup>9</sup>R. A. Kruger, K. D. Miller, H. E. Reynolds, W. L. Kiser, Jr., D. R. Reinecke, and G. A. Kruger, "Contrast enhancement of breast cancer in vivo using thermoacoustic CT at 434 MHz," *Radiology* **216**, 279–283 (2000).
- <sup>10</sup>H. Jiang, *Diffuse Optical Tomography: Principles and Applications* (CRC, Florida, 2011).
- <sup>11</sup>M. Pramanik, G. Ku, C. Li, and L. V. Wang, "Design and evaluation of a novel breast cancer detection system combining both thermoacoustic (TA) and photoacoustic (PA) tomography," *Med. Phys.* **35**(6), 2218–2223 (2008).
- <sup>12</sup>R. A. Kruger, R. B. Lam, D. R. Reinecke, S. P. Del Rio, and R. P. Doyle, "Photoacoustic angiography of the breast," *Med. Phys.* **37**(11), 6096–6100 (2011).
- <sup>13</sup>X. Li, L. Xi, R. Jiang, L. Yao, and H. Jiang, "Integrated diffuse optical tomography and photoacoustic tomography: Phantom validations," *Biomed. Opt. Express* **2**, 2348–2353 (2011).
- <sup>14</sup>L. Yao, Y. Sun, and H. Jiang, "Quantitative photoacoustic tomography based on the radiative transfer equation," *Opt. Lett.* **34**(12), 1765–1767 (2009).
- <sup>15</sup>C. Li and H. Jiang, "Imaging of particle size and concentration in heterogeneous turbid media with multispectral diffuse optical tomography," *Opt. Express* **12**(25), 6313–6318 (2004).
- <sup>16</sup>H. Jiang, N. V. Iftimia, Y. Xu, J. A. Eggert, L. L. Fajardo, and K. L. Klove, "Near-infrared optical imaging of the breast with model-based reconstruction," *Acad. Radiol.* **9**(2), 186–194 (2002).
- <sup>17</sup>V. G. Andreev, A. A. Karabutov, and A. A. Oraevsky, "Detection of ultrawide-band ultrasound pulses in optoacoustic tomography," *IEEE Trans. Ultrason. Ferroelectr. Freq. Control* **50**, 1383–1390 (2003).
- <sup>18</sup>M. Xu and L. V. Wang, "Analytic explanation of spatial resolution related to bandwidth and detector aperture size in thermoacoustic or photoacoustic reconstruction," *Phys. Rev. E* **67**, 056605 (2003).
- <sup>19</sup>C. G. A. Hoelen and F. F. M. de Mul, "Image reconstruction for photoacoustic scanning of tissue structures," *Appl. Opt.* **39**, 5872–5883 (2000).